

High-Efficiency Silicon Photonic Modulator Using Coupled Bragg Grating Resonators

Omid Jafari, Hassan Sepehrian, *Student Member, IEEE*, Wei Shi, *Member, IEEE, Member, OSA*, and Sophie LaRochelle, *Senior Member, IEEE, Fellow, OSA*

Abstract— We propose a novel design of a silicon photonic modulator that has a high modulation efficiency and that is tolerant to temperature variations. A series of phase-shifted Bragg gratings are placed in each arm of a Mach-Zehnder interferometer in order to provide enhanced phase modulation. The slow light effect in these ultra-compact coupled resonators improves phase modulation efficiency compared to conventional silicon phase shifters. These Bragg grating cavities are designed such that the optical bandwidth is increased compared to other coupled resonators such as micro-rings. This improved bandwidth reduces the temperature sensitivity of the devices. We present in detail how to optimize these modulators considering properties such as modulation efficiency ($V_{\pi} \times L$), optical modulation amplitude (OMA), and optical bandwidth ($\Delta\lambda_{BW}$); the latter property determining the operating temperature range (ΔT). As examples, we present two designs that meet different target specifications for short-reach or long-haul applications. We further provide a model, based on coupled mode theory, to investigate the dynamic response of the proposed modulators. A large signal analysis is performed using finite difference time domain (FDTD) in order to simulate on/off keying (OOK) modulation and eye diagrams up to 110 Gb/s.

Index Terms— Optical communications, Silicon photonic modulator, Bragg grating modulator, Resonator-based modulator, Coupled-cavity Bragg grating.

I. INTRODUCTION

Optical communications are the backbone of modern communication systems that provide high-speed access and exchange of data stored around the world. Research in electro-optic (EO) modulators is currently playing a critical role in the ongoing development of future optical interconnects needed to improve the performance of data communication networks [1]–[2]. Silicon photonic (SiP) modulators are currently being considered as a key technology because of their compatibility with complementary metal oxide semiconductor (CMOS) fabrication processes, which ensures low-cost large-scale production. However, the performance of silicon photonic modulators is impaired by the lack of significant EO or electro-absorption effects [2]. Plasma dispersion, therefore, becomes

the preferred means to modulate the refractive index of silicon. Conventional silicon Mach-Zehnder modulators (MZM) require long phase shifters combined to travelling RF waveguides to achieve the required phase modulation. These MZMs are typically characterized by low efficiency and high power consumption [3]–[7]. Notwithstanding, conventional MZM have a wide optical bandwidth, which also translates into a large temperature operating range. MZMs further present the significant advantage of small chirp when operated in a push-pull configuration. Resonator-based SiP modulators (RBMs) [8]–[12], in contrast to conventional MZMs, have a more compact footprint and lower power consumption. This results from the resonance phenomenon, and its associated cavity lifetime, that leads to phase-shifts that are much more sensitive to the applied voltage, resulting in sharply increased modulation efficiency. However, RBMs generate chirped pulses and are very sensitive to temperature variations due to their narrow optical bandwidth. It is worth pointing out that the active stabilization of micro-ring modulators (MRM) consumes significantly more energy than the modulator driver [8].

Combining resonators and a Mach-Zehnder interferometer (MZI) structure can improve modulator performance. In [13]–[14], ring resonators are introduced into the arm of a MZI to increase modulation efficiency. This further makes the device more compact, but is achieved at the expense of a reduced optical bandwidth, which raises its temperature sensitivity significantly. Cascaded rings have been inserted in each arm of a MZI to overcome optical bandwidth limitations; however, this design also suffers from free spectral range (FSR) limitations [15]. In another approach, photonic crystal waveguides (PCW) were proposed for phase modulation enhancement that achieve high delay-bandwidth product [16]–[18]. However, PCW-based designs are very challenging for large-wafer fabrication processes with UV lithography and their performance is highly sensitive to parameter variations. In [19], it is reported that fluctuation of the hole radius by only 1% results in a propagation loss of 150 dB/cm. Consequently, most PCW-based devices typically require highly accurate fabrication process such e-beam lithography [20]. Bragg grating devices, which are 1-D photonic crystals, are less sensitive to fabrication errors and are routinely fabricated with CMOS compatible fabrication process using UV lithography [11], [12], [21]–[25].

In this paper, we propose a novel SiP modulator design based on phase modulation enhancement in a MZI using coupled

Centre d'optique, photonique et laser (COPL), Department of Electrical and Computer Engineering, Université Laval, Québec, QC G1V 0A6, Canada (e-mail: omid.jafari.1@ulaval.ca; hassan.sepehrian.1@ulaval.ca; wei.shi@gel.ulaval.ca; sophie.larochelle@gel.ulaval.ca)

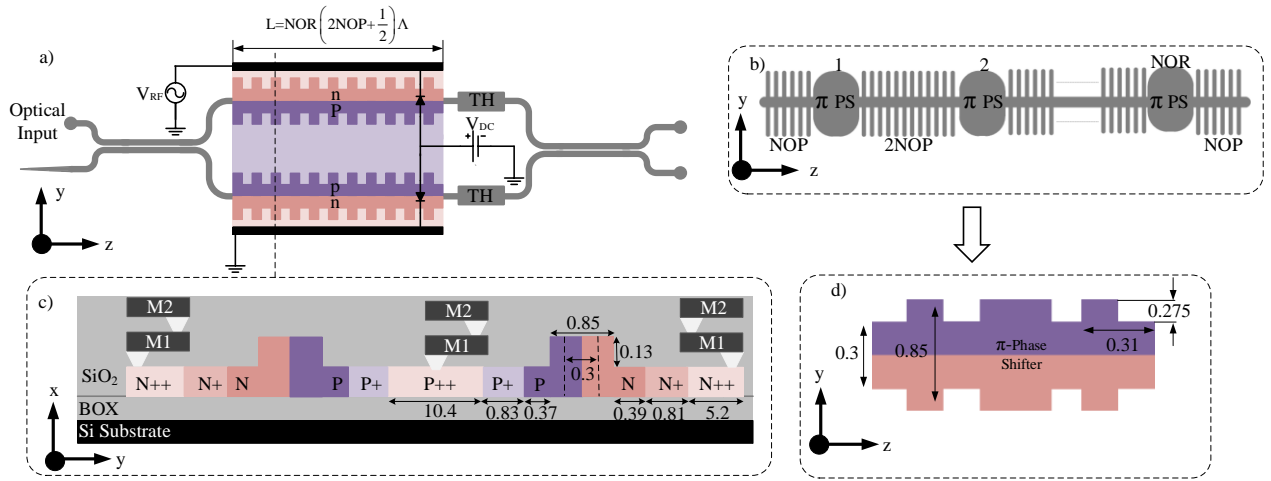


Fig. 1. Schematic of the BGR-MZM showing (a) the configuration of the BGR-MZM, (b) the phase-shifted IBG present in each arm, (c) the cross-section showing the p-n junction and the three doping levels, and (d) the phase-shifted IBG cavity. TH: Thermal element, PS: Phase-shifted cavity, M1: Metal 1, M2: Metal 2, NOP: Number of periods of the resonator mirrors on each side, NOR: number of resonators. All dimensions are shown in micrometers.

Bragg grating resonators (BGRs). This modulator exhibits properties that achieve a compromise between the high modulation efficiency of MRM and the wide optical bandwidth of conventional MZM. The coupled BGRs are used in low-dispersion slow light (LDSL) regime and, compared to other RBMs, they show an improved delay-bandwidth product, which is the fundamental limitation of slow-light-based devices. High time delay, corresponding to large group index, offers modulation enhancement. Wider optical bandwidth results in lower sensitivity to temperature. Consequently, the proposed design is more stable and has a broader operating temperature range than the MRM. In comparison to conventional MZMs, it requires a lower peak-to-peak voltage (V_{pp}) and offers a much more compact footprint. Furthermore, due to its short length, the modulator can be operated with lumped electrodes, even at high speed.

In the following sections, we present detailed modeling and optimization of the modulator structure. The phase enhancement, created by the superstructured integrated Bragg grating (IBG), is analyzed in order to optimize the number of resonators (NORs) and grating periods. Simulations are done considering different performance indicators such as the figure of merit (FOM) $V_{\pi} \times L$, OMA at the operational wavelength, λ_p , and operating temperature range. The next section presents the operating principle of the modulator and introduces the various parameters. In section III, the modulator is optimized using its static response characteristics. Simulations of the dynamic response of the whole structure then follow in section IV. Details on the numerical methods are included in the Appendix. Finally, a conclusion follows in section V.

II. MODULATOR OPERATING PRINCIPLE

In silicon waveguides, light propagates with a group velocity equal to c/n_g where c is the speed of light in vacuum and the group index, n_g , is typically equal to ~ 4 for rib-waveguides. The group index depends on the first-order dispersion that can be sharply enhanced by the presence of a resonance [26]. Ring resonators [27]–[29], photonic crystals [30], [31], and Bragg

gratings [32]–[34] are all resonating structures that can result in slow-light behavior for optical frequencies close to their band gap. The cost associated with the beneficial attributes of slow light is that the second-order dispersion also increases, consequently making the optical bandwidth narrower [26], [35]. Therefore, using slow light to improve the efficiency of modulators could have important benefits for optical interconnects by offering a solution with high speed, small size, and low energy consumption. However, optical structures providing wider optical bandwidth and improved stability must first be demonstrated.

Fig. 1 (a) shows the configuration of the proposed modulator that we will refer to as a Bragg grating resonator assisted MZM (BGR-MZM). To take advantage of slow light, one superstructured IBG with a uniform period is inserted in each arm. These IBGs have coupled resonators created by introducing π -phase shifts as shown in Fig. 1 (b). The coupled resonators are designed with a low-quality factor to make the optical bandwidth wider while maintaining a large phase enhancement. In other words, each resonator operates in the LDSL regime to achieve a wide optical bandwidth; thereafter, the large n_g is achieved by placing a series of coupled resonators. Therefore, the modulation efficiency is similar to other RBMs but with a higher optical bandwidth, conferring a larger achievable temperature operating range without thermal stabilization. Lastly, the whole IBG length (L) remains quite small, even when a large number of resonators are inserted, because the IBGs are designed with a strong coupling coefficient that is obtained by large sidewall corrugations.

In [15], micro-ring resonators have been similarly placed in a MZI (MRR-MZM) to increase modulation efficiency. These were cascaded resonators rather than coupled ones. Compared to MRR-MZMs with cascaded resonators, the proposed BGR-MZM with coupled resonators exhibits a larger optical bandwidth. Also, when BGR-MZMs are implemented with strong corrugations, the footprint area is no larger than a MZM with back-to-back Y-junctions. Indeed, inserting IBGs requires only the introduction of a very small waveguide length of a few

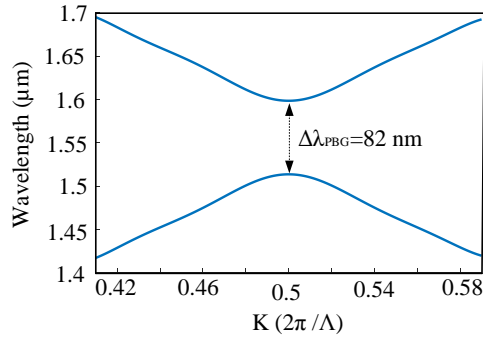


Fig. 2. Simulated photonic band-structure of the IBG.

hundred micrometers in the MZI arms. The small size also makes the design more robust to fabrication variations that typically occur over a large scale. In the case of MRR-MZM, it is possible to make the footprint quite small, but MRRs with small radius are more susceptible to fabrication errors.

III. DESIGN AND OPTIMIZATION

In this section, we first calculate the static response of the BGR-MZM and then optimize the IBG design through numerical simulations. We consider IBGs with a uniform period of $\Lambda=310$ nm in each arm. As can be seen in Fig. 1 (c) and (d), the gratings are designed using sidewall corrugations with a duty cycle of 50% in a ridge waveguide having a maximum width of 850 nm, minimum width of 300 nm, ridge height of 220 nm, and slab height of 90 nm. Each resonator of the Bragg grating structure is composed of two mirrors with NOP periods and a phase shift of half a period, resulting in a total length for the structure that scales with NOR as indicated in Fig. 1 (a). The number of periods (NOP) and the NOR are varied to obtain the desired modulator properties. The total corrugation amplitude and average waveguide width are 550 nm and 575nm, respectively. Similar corrugation amplitude and average waveguide width have, for example, been reported in [32]. The aforementioned parameters are considered constant during the optimization of the NOR and NOP. Under the application of the driving voltage, we assume that the modulator is operated in a single drive push-pull configuration. Thermal elements are

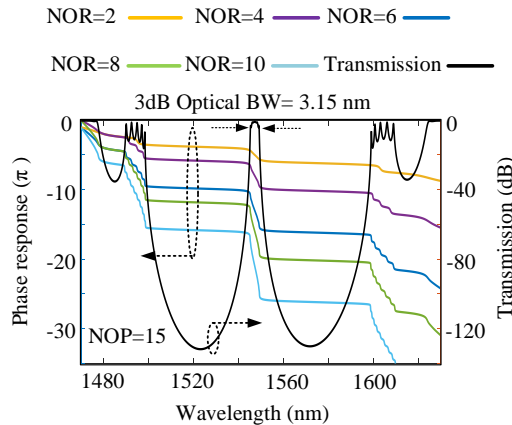


Fig. 3. Power transmission (black line) and phase response (colored lines) of an IBG with multiple phase shifts. The transmission is calculated for NOP=15 and NOR=6. Phase shifts are plotted for NOP=15 and different values of NORs. NOR: number of resonators, NOP: number of periods.

placed in both arms in order to adjust the modulator phase bias. The p-n junctions are formed over the entire IBG length.

3.1 Spectral Response

After the 3-dB adiabatic coupler, the input light goes through an IBG in each arm of the MZI. To determine the transmission power and phase responses of the IBGs, we use the transfer-matrix implementation of the solutions to the coupled-mode equations (see for example [35] and details in Appendix A). To estimate the grating coupling coefficient, κ , we first calculate the IBG photonic band gap, $\Delta\lambda_{PBG}$, using a commercial software (FDTD-Lumerical). The coupling coefficient for IBG modeling is extracted using [36],

$$\kappa = \frac{\pi n_g \Delta\lambda_{PBG}}{\lambda_c^2} \quad (1)$$

where λ_c is the central wavelength of $\Delta\lambda_{PBG}$ and n_g is the average group index. Fig. 2 shows the band-structure of the IBG. The photonic bandgap, $\Delta\lambda_{PBG}=82$ nm, corresponds to a coupling coefficient of $\kappa = 402370 \text{ m}^{-1}$.

The goal of using an IBG with a large photonic band gap is that a lower number of periods is needed to achieve the required 3-dB optical bandwidth, resulting in an extremely short IBG length that translates into a low modulation power. In other words, we keep grating strength ($\kappa \times L$) high but grating length small. It is noteworthy that an IBG with strong corrugation is likely to exhibit significant radiation loss, and consequently a higher attenuation coefficient per unit length but the total average loss remains in reasonable range as will be discussed in section 3.5.

Fig. 3 (solid black line) shows the spectral response of an IBG with multiple phase shifts. The transmission amplitude is plotted for NOP=15 and NOR=6. The 3-dB optical bandwidth is 3.15 nm, confirming that the proposed modulator will have improved thermal stability compared to usual RBMs.

3.2 Phase response

When a voltage is applied to the IBGs, modification of the width of the depletion region causes a variation of the waveguide refractive index. For high-speed operation, the p-n junction is operated in a carrier depletion mode using a reverse bias [37]. Fig. 4 plots the variation of the effective refractive index, Δn_{eff} , as a function of reverse bias voltage modeled as in

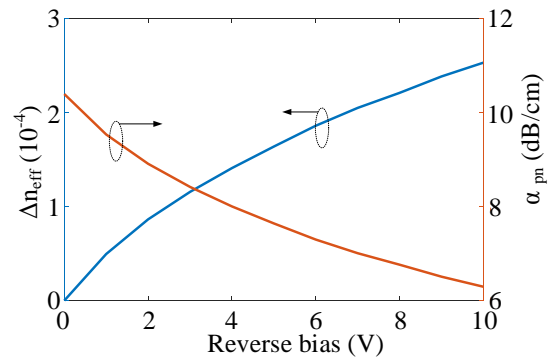


Fig. 4. Variation of the rib waveguide effective refractive index and absorption loss of pn junction as a function of reverse voltage for simple phase shifters.

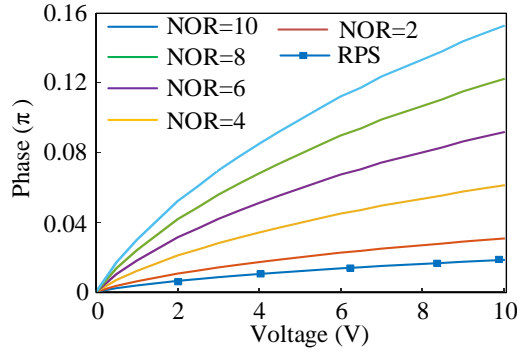


Fig. 5. Phase variation as a function of applied reverse voltage for NOP=15 and various NORs. RPS: a reference phase-shifter (waveguide with p-n junction that has a length equal to the length of the IBG with NOR=6 and NOP=15. NOR: number of resonators, NOP: number of periods.

[38]. As can be seen, Δn_{eff} remains below 2.5×10^{-4} due to the weak plasma dispersion effect in silicon and to the small overlap between the optical mode and the depletion region in the lateral-junction configuration.

Fig. 3 shows how resonators can improve the phase modulation. The colored lines represent the phase of the transmitted signal for NOP=15 and different values of NOR. The phase response is becoming steeper with increasing NOR for wavelengths transmitted through the transmission peak created by the resonating cavities. We define the operational wavelength, λ_p , as the central peak wavelength, which is, in the present case, $\lambda_p = 1547.3$ nm. Therefore, phase modulation enhancement is achieved, which means that a lower V_{pp} is needed to reach the required phase modulation. Fig. 5 shows the absolute value of the transmitted phase modulation as a function of voltage for a NOP of 15 and various NORs. Comparison to the reference phase shifter in the conventional rib waveguide (solid blue line with square marker) shows a substantially increased slope in the phase response.

3.3 Phase modulation enhancement

To further investigate the LDSL regime, we examine Fig. 6 that shows the spectral dependence of the calculated n_g for NOR=6 and NOP=15 on each side of the resonators. The group index curve shows a plateau near the peak wavelength with $n_g \sim 20$, which is several times larger than the n_g of a rib waveguide. On the edge of the passband, n_g reaches values near 60, but over a narrow optical bandwidth, which makes the operation of the modulator at these wavelengths impractical.

To quantify the slow light effect, we introduce an enhancement factor, γ , which is defined as the ratio between the values of the derivative of the transmitted phase with respect to the applied voltage for an IBG with multiple resonators to the derivative calculated for a conventional phase shifter (waveguide with p-n junction) of the same length. We write

$$\gamma = \frac{\frac{\partial \phi}{\partial V}}{\frac{\partial \phi_w}{\partial V}} \quad (2)$$

where V is the applied voltage, and ϕ and ϕ_w are the transmitted phase of the IBG and of a simple rib waveguide, respectively.

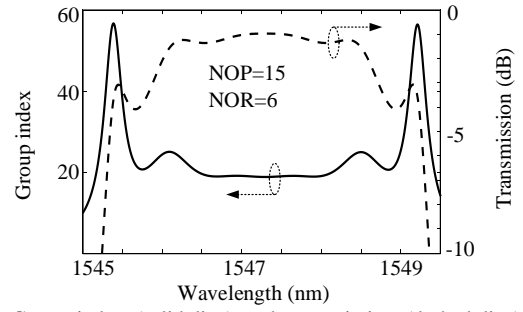


Fig. 6. Group index (solid line) and transmission (dashed line) versus wavelength for NOP=15 and NOR=6. NOR: number of resonators, NOP: number of periods.

Fig. 7 (a) shows γ as functions of both NOP and NOR. As can be seen, a larger NOP results in a more efficient modulator. As shown in Fig. 7 (b), this enhancement comes at the cost of reduced 3-dB optical bandwidth because of the increased quality factor of the resonators. Therefore, the choice of NOP is a compromise between the operational temperature range and modulation efficiency, i.e., time delay-bandwidth product. Fig. 8 shows the aforementioned tradeoff between bandwidth and time delay with respect to NOP for various NORs. From Fig. 7 (a) and (b), we also see that the enhancement factor and 3-dB optical bandwidth remain almost constant as the number of cavities is increased. More precisely, when the NOR is increased, some small ripples appear in the amplitude response, but the changes in the 3-dB optical bandwidth are negligible.

To examine modulation efficiency, we plot in Fig. 7 (c) the value of the derivative of the transmitted phase with respect to the applied voltage at λ_p . We refer to this quantity as the efficiency factor. Fig. 7 (c) shows the variation of the efficiency factor with respect to both NOP and NOR. From Fig. 7 (b) and

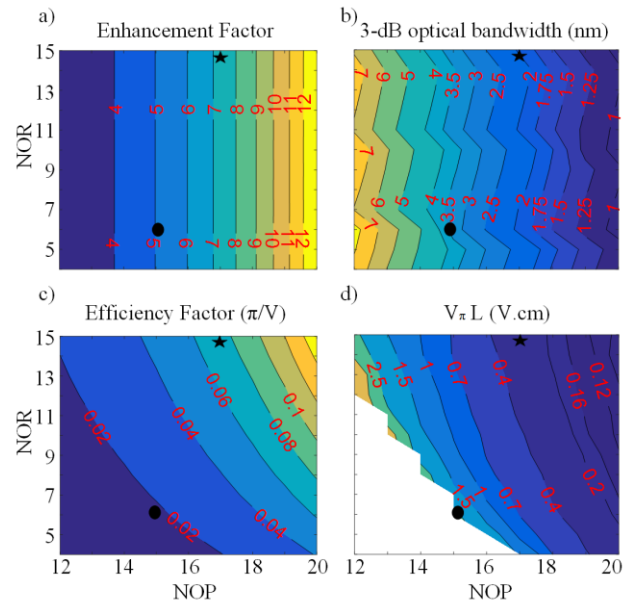


Fig. 7. (a) Enhancement factor γ , and (b) 3-dB optical bandwidth of the transmission peak. (c) Efficiency factor and (d) FOM; all as functions of NOR and NOP. Star and dot markers show two designs chosen for long- and short-distance applications respectively.

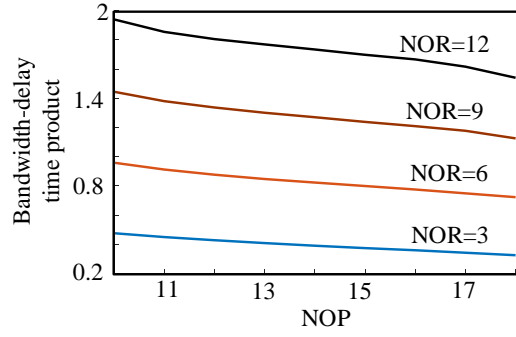


Fig. 8. Bandwidth-delay product as a function of NOP for various NORs.

(c), it is clear that adding resonators improves phase modulation (larger time delay or larger n_g) while the 3-dB optical bandwidth remains almost constant, leading to an enhanced time delay-bandwidth product. Fig. 8 confirms the product enhancement. However, a larger NOR results in a higher optical loss that will be considered in the discussion of OMA.

The FOM defined as $V_\pi \times L$ is often used to characterize the efficiency of a modulator. Fig. 7 (d) shows the FOM calculated as functions of NOR and NOP; note that NOP is directly linked to the enhancement factor (Fig. 7 (a)) and the NOR is mostly related to the IBG length L . A given FOM can therefore be achieved with different sets of NOR and NOP. For example, to design a modulator with a FOM of 1 V.cm, we can choose NOR=13 and NOP=15 ($L=121 \mu\text{m}$, $\gamma=5$), NOR=10 and NOP=16 ($L=100 \mu\text{m}$, $\gamma=6$), or NOR=7 and NOP=17 ($L=74 \mu\text{m}$, $\gamma=7.2$). From Fig. 7 (b), their 3-dB bandwidths are approximately 4 nm, 3 nm, and 2 nm, respectively. If we target a smaller enhancement factor (corresponding to lower NOP), the 3-dB optical bandwidth will be larger resulting in a more stable operation of the device. In this case however, the NOR will have to be increased in order to achieve a specific phase modulation.

3.4 Optical Modulation Amplitude (OMA)

These IBGs are phase modulators that need to be inserted in a MZI to produce amplitude modulation. The quality of the amplitude-modulated signal is thus examined by calculating the OMA of the BGR-MZM at λ_p . In this section, we calculate the OMA from the static response, i.e., as a function of DC voltage. The dynamic response will be examined in section IV. The output power of the MZI is calculated assuming ideal input and output 3-dB power splitters,

$$P_{out} = P_{in} \exp(-\alpha L) \cos^2(\Delta\phi_v) \quad (3)$$

$$\Delta\phi_v = \frac{k_0 \Delta n_{eff} (V) \gamma L + \Delta\phi_0}{2} \quad (4)$$

where P_{in} is the input power and α is the propagation loss coefficient. The total phase difference between the two MZI arms is $\Delta\phi_v$. $\Delta\phi_0$ represents the initial phase difference between the two arms. The phase modulation is calculated from the variation of the waveguide refractive index, Δn_{eff} , multiplied by γ . Finally, k_0 is the wavenumber equal to $2\pi/\lambda_0$. At the BGR-MZM output, the OMA is calculated using

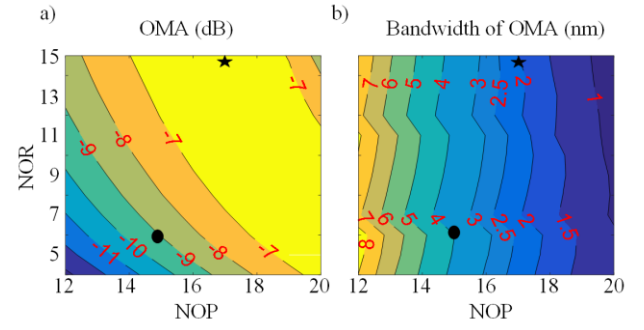


Fig. 9. (a) OMA and (b) 3-dB OMA bandwidth as functions of NOR and NOP. Star and dot markers are the designs chosen for long- and short-distance applications respectively as in Fig. 7.

$$OMA = 10 \log \left(\frac{Output Power_{on} - Output Power_{off}}{Input Power} \right) \quad (5)$$

Fig. 9 (a) shows the OMA at λ_p as functions of NOR and NOP with an applied voltage V_{pp} of 4 V on each arm, V_{bias} is -2 V, and $\Delta\phi_0$ is 0.5π . The lower OMA (bottom-left) comes from the lower efficiency factor, which results in a closed eye. The opposite corner (top right) also shows a lower OMA although this corresponds to a region with a high-efficiency factor. In this case, it is the long IBG length that induces high loss, which reduces the power level of bits “1”. Consequently, there are some IBG parameter sets (NOR and NOP) that maximize the OMA (yellow color in Fig. 9 (a)). High OMA is a key parameter in long-distance applications.

The 3-dB OMA spectral bandwidth (BW-OMA) can be used to examine the stability of the modulator operation with respect to temperature variations, i.e. a larger BW-OMA corresponds to a lower thermal sensitivity. Fig. 9 (b) shows the BW-OMA versus NOR and NOP for a V_{pp} of 4 V on each arm, V_{bias} is -2 V, and $\Delta\phi_0 = 0.5\pi$. From Fig. 9 (b) and Fig. 7 (b), it can be seen that the BW-OMA variations follow the 3-dB optical bandwidth of the transmission peak.

3.5 Loss

The on-chip loss of the modulator comes mostly from the absorption due to the carriers in the pn-junction and the scattering loss produced by the IBG with strong corrugations. The simulated absorption loss of the pn junction for a simple phase shifter is plotted in Fig. 4, showing ~9 dB/cm absorption loss for bias voltage of -2 V [38]. Assuming that the absorption loss increases linearly with the enhancement factor and considering an average enhancement factor of 8 (see Fig. 7 (a)), the absorption loss of our structure is 72 dB/cm. Furthermore, according to Xu. *et al.* [39], at up to 160 nm corrugation, no significant excess loss in IBGs is observed compared to simple waveguides. Since the corrugations of the IBGs in our proposed modulator structure are significantly larger, we performed 3D FDTD simulations to estimate loss. Due to memory limitations, we simulated a uniform IBG with a length of about 15.5 μm (50 periods) and corrugations of 550 nm (275 nm on each side). The simulated device was surrounded by perfectly matched layer (PML) boundaries and power monitors were placed at the IBG output and the input to calculate the transmission (T) and reflection (R). The IBG excess loss calculated as 1-(T+R) was

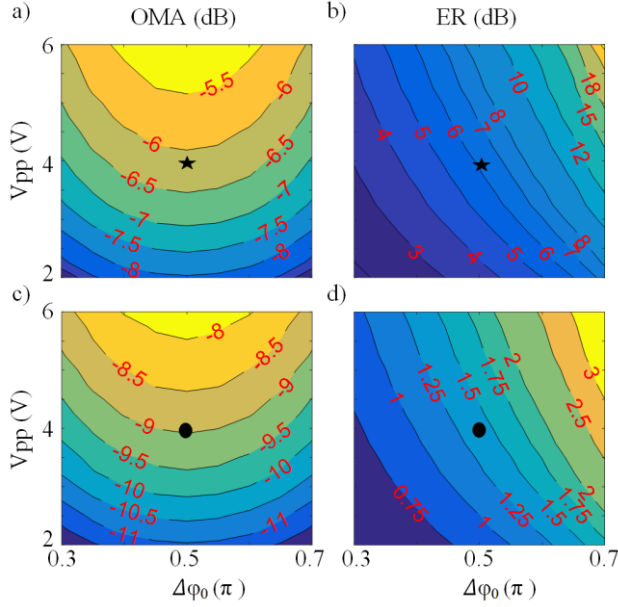


Fig. 10. (a) OMA and (b) ER as functions of V_{pp} and $\Delta\phi_0$ for NOP=17 and NOR=15. (c) OMA and (d) ER as functions of V_{pp} and $\Delta\phi_0$ for NOP=15 and NOR=6. Star and dot markers are the designs chosen for long- and short-distance applications respectively (as in Fig. 7 and Fig. 9).

negligible (<0.003) both outside its bandgap and in its stopband over the spectral bandwidth where it is operated as a modulator. As a best estimate, we therefore assume that the results of Xu *et al.* are also valid in the case of our device and set the loss of the IBG structure of our modulator at 2.5 dB/cm, similarly to the scattering loss of a simple waveguide as in [39]. Now, considering an average enhancement factor of 8, and assuming a linear relationship between the enhancement factor and the scattering loss, our best estimate for the scattering loss of the modulator is 20 dB/cm. Despite this large loss, the total loss of our modulator remains reasonable because of the very small lengths involved. Considering a typical phase shifter length of 100 μm , the loss of the modulator structure is of the order of 1 dB.

3.6 Examples of modulator designs

We now examine two specific modulator designs: [NOR=15, NOP=17] and [NOR=6, NOP=15]. Their characteristics are marked as a black-star and a black-dot respectively in Fig. 7 and Fig. 9. The first design, with a larger number of resonators and grating period, achieves higher OMA but requires higher driving power due to the longer IBG length ($L=160 \mu\text{m}$). The second design is a compact modulator ($L=56 \mu\text{m}$) that compromises on the OMA to reduce driving power requirement. The longer design would, therefore, be appropriate for systems requiring higher performance, such as high-order modulation formats, while the shorter one would be of interest for short-reach data links.

When optimizing the electrical bias, both OMA and power consumption should be considered. Power consumption (P_C) is a function of V_{pp} and is written $P_C = \frac{1}{4} CV_{pp}^2$ for OOK modulation. The driving voltage, V_{pp} , decreases when the NOR

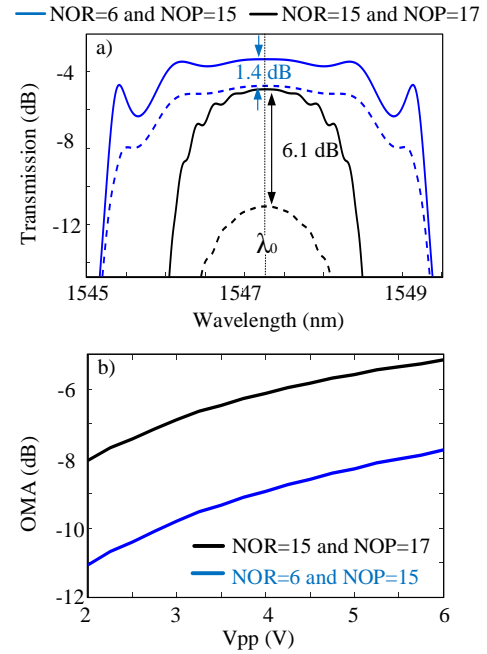


Fig. 11. (a) Static optical modulation calculations for NOR=6 and NOP=15 (blue curves); and for NOR=15 and NOP=17 (black curves), (b) OMA as a function of voltage for these two designs. In (a), dashed-line and solid-line show off and on states, respectively.

increases but this increase in L also results in a larger capacitance. Nonetheless, to lower power consumption, it is beneficial to choose V_{pp} as low as possible. Fig. 10 (a) and (b) show OMA and extinction ratios (ER) at λ_P as functions of $\Delta\phi_0$ and V_{pp} on each arm. We consider that V_{bias} is $-V_{pp}/2$. Unsurprisingly, Fig. 10 (a) demonstrates that the highest OMA is reached when $\Delta\phi_0=0.5\pi$, called the quadrature point. Therefore, biasing the modulator at the quadrature point ensures that the lowest V_{pp} will be needed to reach a given OMA, and will result in the lowest power consumption. Note that the ER increases as functions of both $\Delta\phi_0$ and V_{pp} as indicated in Fig. 10 (b). We consider $\Delta\phi_0=0.5\pi$ and $V_{pp}=4 \text{ V}$ in all the simulation results presented below. This corresponds to the black-star markers in Fig. 10 (a) and (b) for NOP=17 and NOR=15. Fig. 10 (c) and (d) demonstrate similar results for the second design. In Fig. 7, Fig. 9, and Fig. 10, simulations are performed with NOP and NOR that are integer numbers which would result in block type graphs. To aid in identifying the trends, we smoothed the block type color graph using the Contourf command in MatLab.

Fig. 11 (a) shows the modulation of the transmission for these two designs using $V_{pp}=4 \text{ V}$ on each arm, $V_{bias}=-2 \text{ V}$, and $\Delta\phi_0=0.5\pi$. As can be seen, the ON/OFF ERs are 6.1 dB and 1.4 dB. Fig. 11 (b) shows how OMA is improved when increasing V_{pp} . Furthermore, in Fig. 11 (a), we note that the BW-OMA is reduced, from approximately 4 nm to 2 nm, when increasing the enhancement factor by using larger NOPs. Fig. 12 (a) and (b) zoom on the OMA spectrum of both designs and show the impact of temperature change. For IBGs in silicon waveguides, typical peak wavelength shift with temperature is $\Delta\lambda/\Delta T = 80 \text{ pm/K}$ [8]. A 3-dB reduction of operating OMA, therefore, leads to a temperature operating range of $\sim \pm 12.5 \text{ K}$ and $\sim \pm 25 \text{ K}$ for

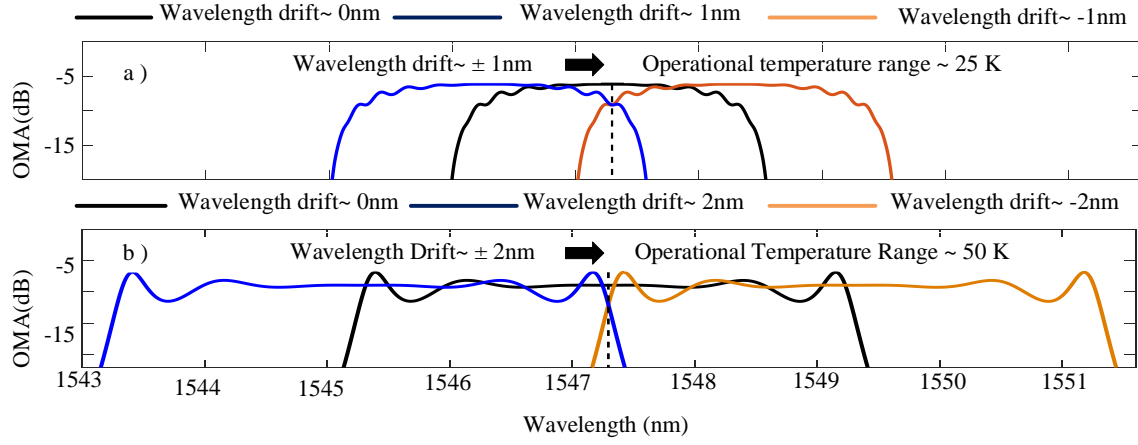


Fig. 12. OMA spectra calculated for a) NOR=15 and NOP=17 (black line), and (b) NOR=6 and NOP=15 (black line). In (a), OMA calculated with temperature variations of $\Delta T = -12.5$ K (blue line) and $\Delta T = 12.5$ K (red line) are also plotted. In (b), OMA calculated with temperature variations of $\Delta T = -25$ K (blue line) and $\Delta T = 25$ K (red line) are also plotted.

the two designs as shown in Fig. 12. For comparison, a single resonator MRM can tolerate only a few kelvins of temperature variations [8].

IV. DYNAMIC RESPONSE

In this section, we develop a dynamic model of BGR-MZMs to examine their frequency response. The model is based on the time-dependent coupled-mode equations (see for example [40] and [41]) that take into account the response of the resonating structure. The differential equation set is solved using FDTD in

MatLab [42]. Because of memory limitation, we numerically investigate only the second design that has a shorter length with NOP=15 and NOR=6. The IBG starts at $z=0$ and ends at $z=L$. The phase shifts are located at $z = L/12, 3L/12, 5L/12, 7L/12, 9L/12, 11L/12$. We write the input signal at the IBG input as $E_{cw} = f_0 \exp(i(\beta z - \omega t))$. The equations representing the propagation of the envelopes of the forward and backward propagating mode fields (F and B , respectively), in the waveguide section with a Bragg grating structure (BGS) and in the sections where the waveguide is uniform to create a phase-shift segment (PSS), are as follow,

$$\text{BGS} \begin{cases} \frac{\partial F}{\partial z} + \frac{n_{eff}(t)}{c} \frac{\partial F}{\partial t} = i \kappa B \exp(-i 2\Delta\beta z) \\ \frac{\partial B}{\partial z} - \frac{n_{eff}(t)}{c} \frac{\partial B}{\partial t} = -i \kappa F \exp(i 2\Delta\beta z) \end{cases} \quad (6-1)$$

$$\text{PSS} \begin{cases} \frac{\partial F}{\partial z} + \frac{n_{eff}(t)}{c} \frac{\partial F}{\partial t} = 0 \\ \frac{\partial B}{\partial z} - \frac{n_{eff}(t)}{c} \frac{\partial B}{\partial t} = 0 \end{cases} \quad (6-2)$$

where c is the speed of light in vacuum. Also, $n_{eff}(t)$ is the waveguide effective index described as $n_{eff}(t) = n_{eff} - \Delta n_{eff}(t)$, where n_{eff} is effective index of unperturbed waveguide and $\Delta n_{eff}(t)$ is the time-dependent perturbation resulting from the applied voltage as represented in Fig. 4. Eq. 6-1 and Eq. 6-2 can be rewritten using normalized parameters,

$$\text{BGS} \begin{cases} \frac{\partial F}{\partial T} = -\frac{1}{\eta(T)} \left[\frac{\partial F}{\partial Z} - i \kappa L B \exp(-i 2\Delta\beta(T) L Z) \right] \\ \frac{\partial B}{\partial T} = \frac{1}{\eta(T)} \left[\frac{\partial B}{\partial Z} + i \kappa L F \exp(i 2\Delta\beta(T) L Z) \right] \end{cases} \quad (7-1)$$

$$\text{PSS} \begin{cases} \frac{\partial F}{\partial T} = -\frac{1}{\eta(T)} \frac{\partial F}{\partial Z} \\ \frac{\partial B}{\partial T} = \frac{1}{\eta(T)} \frac{\partial B}{\partial Z} \end{cases} \quad (7-2)$$

where,

$$Z = \frac{1}{L} z \quad (8)$$

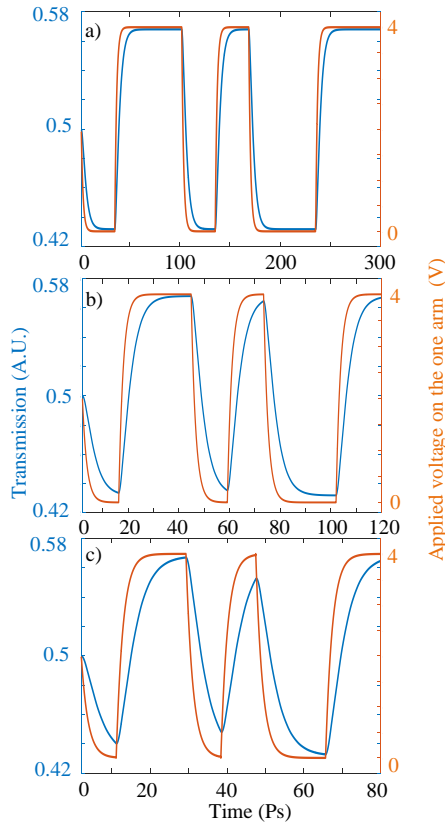


Fig. 13. Time response of BRG-MZM for (a) 30 Gb/s, (b) 70 Gb/s, and (c) 110 Gb/s.

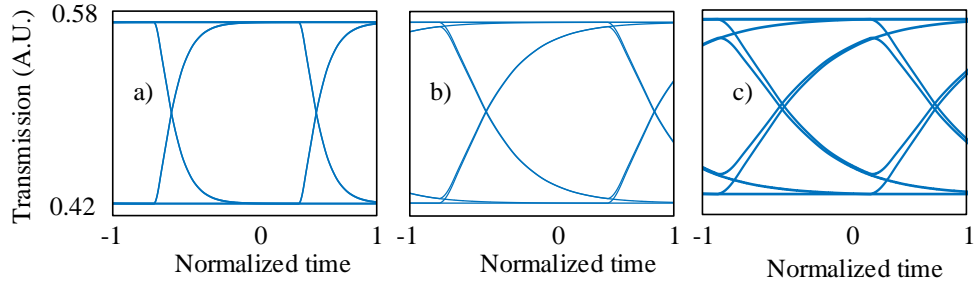


Fig. 14. Eye diagrams calculated for BRG-MZM operated at (a) 30 Gb/s, (b) 70 Gb/s (c) 110 Gb/s.

$$T = \frac{c}{Ln_{eff}}t \quad (9)$$

$$\eta(T) = \frac{n_{eff} - \Delta n_{eff}(t)}{n_{eff}} \quad (10)$$

$$\Delta\beta(T) = \frac{2\pi}{\lambda}(n_{eff} - \Delta n_{eff}(t)) - \frac{\pi}{\Lambda} \quad (11)$$

The numerical solution of the above equations is explained in detail in Appendix B. As input to the simulations, we use pseudorandom binary bit sequence 2^5-1 at different bitrates to evaluate the performance of the modulator. Fig. 13 shows the time response of the BGR-MZM at bitrates of 30 Gb/s, 70 Gb/s, and 110 Gb/s; and their respective eye diagrams are plotted in Fig. 14. It is important to note that the calculated eye diagrams are noiseless and therefore the quality factor of eye diagram would be further reduced in an experimental measurement.

The EO bandwidth of the BGR-MZM is limited by the electrical and optical dynamics that are usually quantified using the RC time constant and the quality factor of the Bragg grating filter (or the photon lifetime, τ). The EO 3-dB cutoff frequency, f_c , of the small signal response of BGR-MZM is estimated by

$$\frac{1}{f_c^2} = \frac{1}{f_{RC}^2} + \frac{1}{f_\tau^2} \quad (12)$$

where f_{RC} represents the cutoff frequency of the RC circuit modeling a reverse biased p-n junction, and f_τ is the optical cutoff frequency, given by $f_\tau = 1/(2\pi\tau)$. The resistance and capacitance of the p-n junction are modeled as in Ref. [38] and are shown as a function of reverse bias in Fig. 15. As can be seen, a junction capacitance of 1.6 PF/cm and resistance of 1.4 Ω .cm are calculated with $V_{DC} = -2$ V, corresponding to $f_{RC} = 69$ GHz. The optical cutoff frequency is estimated by injecting an ultrashort electrical pulse, calculating the transmitted optical pulse using the dynamic model described above, and taking the

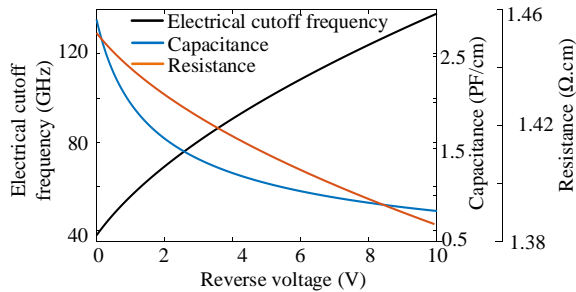


Fig. 15. Capacitance (blue) and resistance (red) of p-n junction as a function of reverse voltage. The resulting electrical cut-off frequency (black) is also shown.

Fourier transform to extract the frequency response. Fig. 16 shows the optical response of the grating structure for various optical detuning ($\Delta\lambda$), showing that $f_c = 49$ GHz for $\Delta\lambda = 0$, which corresponds to $\tau = 3.23$ ps. It can be seen that the optical cutoff frequency is increased if the operational wavelength is tuned away from the resonant wavelength, which however occurs at the expense of reducing both the OMA and the operating temperature range. From Eq. 12, the modulator EO bandwidth is $f_c = 40$ GHz, which is in agreement with the EO bandwidth calculated using the full dynamic model (41 GHz). Fig. 17 shows the dynamic OMA as a function of bitrate. The dot markers are the OMA values calculated with the dynamic model at various bitrates while the line is a guide to the eye.

It is well-known that velocity mismatch between RF and optical signals is another factor that can limit the EO bandwidth [43]–[45]. This effect particularly important when the phase shifter length or the waveguide group index are increased. However, since the length of the simulated phase shifter is quite small ($L = 57.6$ μ m), our dynamic response is not limited by velocity mismatch.

V. CONCLUSION

We proposed a novel SiP modulator design based on a resonant structure with coupled cavities that uses slow light to improve the modulation efficiency and the operating temperature range simultaneously. The key idea is to use an IBG structure operated in transmission as a phase modulator. When inserted in a MZI structure, the resonance enhancement of the phase modulation allows a reduction of the phase shifter length, which improves efficiency in comparison to conventional MZM. Also, the cavities are designed with a low-quality factor to widen the optical bandwidth and significantly increase the tolerance to thermal variations (up to ± 25 K) when

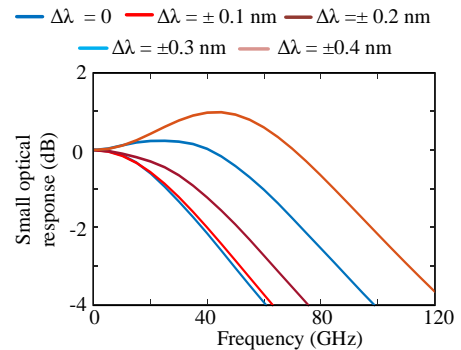


Fig. 16. Small-signal optical response (RC constant is not considered) of BRG-MZM for different frequency detuning.

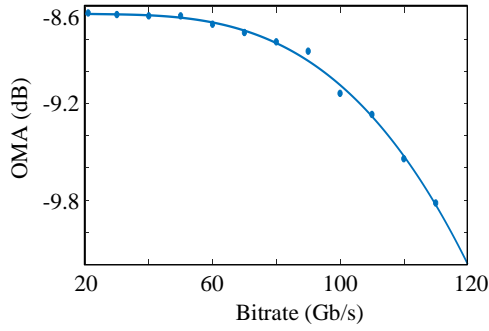


Fig. 17. OMA as a function of bitrate.

compared to modulators based on the use of micro rings. Despite cascading many resonators, the modulator size is remarkably compact due to the use of Bragg gratings with a large photonic band gap. By solving the time-dependent coupled mode equations, we numerically investigated the dynamics of this modulator that exhibits an EO 3-dB cutoff frequency of 40 GHz for the specific design considered. These results show the proposed modulator is promising for low-power, high-speed optical interconnects. The proposed modulator with cascaded resonator waveguides could also be adopted in other 1D photonic crystal structures with stronger dielectric corrugations to achieve a higher bandwidth-delay product and a smaller footprint, but these devices would face the challenge of implementation using UV lithography [46].

APPENDIX

APPENDIX A.

Propagation through an IBG can be calculated using [35],

$$\begin{bmatrix} F(0) \\ B(0) \end{bmatrix} = T \begin{bmatrix} F(L) \\ B(L) \end{bmatrix}, \quad T = (APA)^M \quad (13)$$

where F is the slowly varying envelope of the forward propagating mode, B is the backward propagating one, M is the number of phase-shifts in the IBG, A is transfer matrix that represents the IBGs on each side of the phase-shift resonators, and P is the matrix representing propagation through the phase-shift region. These matrices are defined as,

$$A = \begin{bmatrix} A_{11} & A_{12} \\ A_{21} & A_{22} \end{bmatrix} \quad (14)$$

$$A_{11} = A_{22}^* = \cosh(l\sqrt{\kappa^2 - \Delta\beta^2}) + j \frac{\Delta\beta}{\sqrt{\kappa^2 - \Delta\beta^2}} \sinh(l\sqrt{\kappa^2 - \Delta\beta^2}) \quad (15)$$

$$A_{12} = -A_{21} = j \frac{\kappa}{\sqrt{\kappa^2 - \Delta\beta^2}} \sinh(l\sqrt{\kappa^2 - \Delta\beta^2}) \quad (16)$$

$$P = \begin{bmatrix} P_{11} & P_{12} \\ P_{21} & P_{22} \end{bmatrix} \quad (17)$$

$$P_{11} = P_{22}^* = \exp\left(j\beta \frac{\Lambda}{2}\right) \quad (18)$$

$$P_{12} = P_{21} = 0 \quad (19)$$

where l is the length of grating on one side of a resonator which is $l = N(l \text{ or } 2) \times \Lambda$, where $N1=N2$ is the number of periods on

each side of the cavities and Λ is the grating period. Also, κ is the coupling coefficient, and $\Delta\beta$ represents the wavenumber detuning (or momentum mismatch [35]), which is defined as $\Delta\beta = \beta - \pi/\Lambda$, where β is the propagation constant.

APPENDIX B.

An FDTD method is used to solve Eq. 7 [42]. We take discrete values for Z and T that are defined as $j\Delta Z$ and $n\Delta T$, respectively, where j and n are integers. Therefore, the solution is given at discrete points in the propagation direction. It is important to note that the dynamic model will be more precise if the number of nodes is increased, but at the expense of increased simulation time. In the present case, we consider 7320 nodes, corresponding to $\Delta Z = 1.3361 \times 10^{-4}$. We define the Courant number as $\Gamma = \Delta T / \Delta Z$ [42]. Convergence and stability criteria of the numerical method force the Courant number to be between 0 and 1 [42]. Considering $\Gamma = 0.5$, $\Delta T = 6.83 \times 10^{-5}$ is calculated. The discretized form of Eq. 7 can be written as,

$$\text{BGS} \begin{cases} F_j^{n+1} = F_j^n - \frac{\Delta T}{\eta^n} \times \left[\frac{F_j^n - F_{j-1}^n}{\Delta Z} - i\kappa L B_j^n \exp(-i2\Delta\beta^n L \Delta Z j) \right] \\ B_j^{n+1} = B_j^n + \frac{\Delta T}{\eta^n} \times \left[\frac{B_{j+1}^n - B_j^n}{\Delta Z} + i\kappa L F_j^{n+1} \exp(+i2\Delta\beta^n L \Delta Z j) \right] \end{cases} \quad (20-1)$$

$$\text{PSS} \begin{cases} F_j^{n+1} = F_j^n - \frac{\Delta T}{\eta^n} \left[\frac{F_j^n - F_{j-1}^n}{\Delta Z} \right] \\ B_j^{n+1} = B_j^n + \frac{\Delta T}{\eta^n} \left[\frac{B_{j+1}^n - B_j^n}{\Delta Z} \right] \end{cases} \quad (20-2)$$

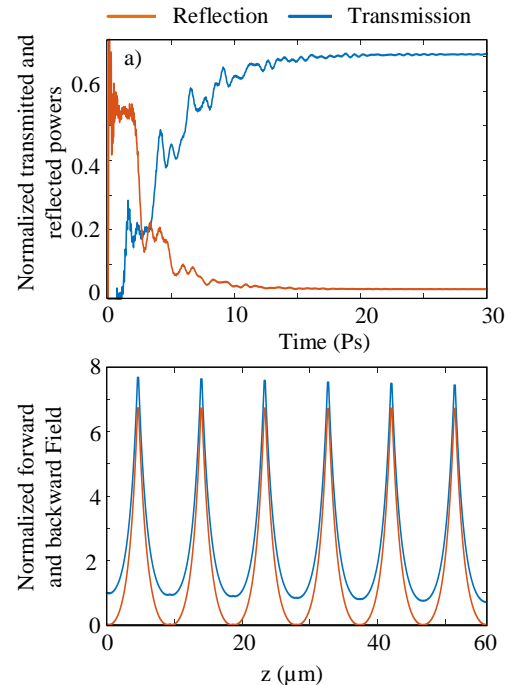


Fig. 18. (a) Transient and steady state responses calculated with FDTD. (b) Initial values of each node are normalized to input power.

where F_j^n is $F(n\Delta T, j\Delta Z)$. The same definition holds true for B_j^n . At $Z=0$ (or $j=1$), the forward field is equal to half of the CW beam and the backward field should be continuous. On the other hand, at $Z=1$ (or $j=7320$), the forward field must be continuous and the backward field is equal to zero. Therefore, the boundary condition for each IBG can be introduced as,

$$F(0,T) = f_0/2, \quad \left. \frac{\partial F(Z,T)}{\partial Z} \right|_{Z=1} = 0 \quad (21-1)$$

$$\left. \frac{\partial B(Z,T)}{\partial Z} \right|_{Z=0} = 0, \quad B(1,T) = 0 \quad (21-2)$$

We first calculate a steady state condition of Eq. 20 using $F_1^1 = 1$, $F_{j \neq 1}^1 = 0$, $B_j^1 = 0$, in order to provide initial values to the nodes. Our model reaches the steady state after approximately 20 ps, as shown in Fig. 18 (a). The initial values of the nodes are illustrated in Fig. 18 (b) where six peaks appear, corresponding to the six phase-shifts.

ACKNOWLEDGMENT

The authors thank Dr. Zhuhong Zhang and his team with Huawei Canada for many useful discussions. This work was supported by Huawei Canada and NSERC (CRDPJ 486716-15).

REFERENCES

- [1] J. Luo and A. K.-Y. Jen, "Highly Efficient Organic Electrooptic Materials and Their Hybrid Systems for Advanced Photonic Devices," *IEEE J. Sel. Top. Quantum Electron.*, vol. 19, no. 6, pp. 42–53, 2013.
- [2] A. Chen and E. Murphy, *Broadband optical modulators: science, technology, and applications*. CRC press, 2011.
- [3] M. Streshinsky *et al.*, "Highly linear silicon traveling wave Mach-Zehnder carrier depletion modulator based on differential drive," *Opt. Express*, vol. 21, no. 3, p. 3818, 2013.
- [4] M. Streshinsky *et al.*, "Low power 50 Gb/s silicon traveling wave Mach-Zehnder modulator near 1300 nm," *Opt. Express*, vol. 21, no. 25, p. 30350, 2013.
- [5] D. Patel *et al.*, "Design, analysis, and transmission system performance of a 41 GHz silicon photonic modulator," *Opt. Express*, vol. 23, no. 11, p. 14263, 2015.
- [6] A. Samani *et al.*, "A Low-Voltage 35-GHz Silicon Photonic Modulator-Enabled 112-Gb/s Transmission System," *IEEE Photonics J.*, vol. 7, no. 3, pp. 1–13, 2015.
- [7] Po Dong, Xiang Liu, S. Chandrasekhar, L. L. Buhl, R. Aroca, and Young-Kai Chen, "Monolithic silicon photonic integrated circuits for compact 100+Gb/s coherent optical receivers and transmitters," *IEEE J. Sel. Top. Quantum Electron.*, vol. 20, no. 4, pp. 150–157, 2014.
- [8] R. Dubé-Demers, S. LaRochelle, and W. Shi, "Ultrafast pulse-amplitude modulation with a femtojoule silicon photonic modulator," *Optica*, vol. 3, no. 6, p. 622, 2016.
- [9] X. Zheng *et al.*, "A high-speed, tunable silicon photonic ring modulator integrated with ultra-efficient active wavelength control," *Opt. Express*, vol. 22, no. 10, p. 12628, 2014.
- [10] Q. Xu, S. Manipatruni, B. Schmidt, J. Shakya, and M. Lipson, "12.5 Gbit/s carrier-injection-based silicon micro-ring silicon modulators," *Opt. Express*, vol. 15, no. 2, p. 430, 2007.
- [11] K. Bédard, A. D. Simard, B. Filion, Y. Painchaud, L. A. Rusch, and S. LaRochelle, "Dual phase-shift Bragg grating silicon photonic modulator operating up to 60 Gb/s," *Opt. Express*, vol. 24, no. 3, p. 2413, 2016.
- [12] M. Caverley, X. Wang, K. Murray, N. A. F. Jaeger, and L. Chrostowski, "Silicon-on-Insulator Modulators Using a Quarter-Wave Phase-Shifted Bragg Grating," *IEEE Photonics Technol. Lett.*, vol. 27, no. 22, pp. 2331–2334, 2015.
- [13] R. Li *et al.*, "An 80 Gb/s Silicon Photonic Modulator Based on the Principle of Overlapped Resonances," *IEEE Photonics J.*, vol. 9, no. 3, pp. 1–11, 2017.
- [14] J. Cardenas *et al.*, "Linearized silicon modulator based on a ring assisted Mach Zehnder interferometer," *Opt. Express*, vol. 21, no. 19, p. 22549, 2013.
- [15] S. Romero-García *et al.*, "High-speed resonantly enhanced silicon photonics modulator with a large operating temperature range," *Opt. Lett.*, vol. 42, no. 1, p. 81, 2017.
- [16] T. Tatebe, T. Baba, Y. Hinakura, and Y. Terada, "Si Photonic Crystal Slow-Light Modulators with Periodic p-n Junctions," *J. Light. Technol. Vol. 35, Issue 9*, pp. 1684–1692, vol. 35, no. 9, pp. 1684–1692, 2017.
- [17] Y. Terada, K. Kondo, R. Abe, and T. Baba, "Full C-band Si photonic crystal waveguide modulator," *Opt. Lett.*, vol. 42, no. 24, p. 5110, 2017.
- [18] H. C. Nguyen, N. Yazawa, S. Hashimoto, S. Otsuka, and T. Baba, "Sub-100 μ m Photonic Crystal Si Optical Modulators: Spectral, Athermal, and High-Speed Performance," *IEEE J. Sel. Top. Quantum Electron.*, vol. 19, no. 6, pp. 127–137, Nov. 2013.
- [19] D. Pergande *et al.*, "Miniature infrared gas sensors using photonic crystals," *J. Appl. Phys.*, vol. 109, no. 8, p. 083117, Apr. 2011.
- [20] A. K. Goyal, H. S. Dutta, and S. Pal, "Recent advances and progress in photonic crystal-based gas sensors," *J. Phys. D: Appl. Phys.*, vol. 50, no. 20, p. 203001, May 2017.
- [21] Xu Wang, M. Caverley, J. Flueckiger, Yun Wang, N. A. F. Jaeger, and L. Chrostowski, "Silicon photonic Bragg grating modulators," in *2014 IEEE Photonics Conference*, 2014, pp. 190–191.
- [22] K. Bédard, A. D. Simard, B. Filion, Y. Painchaud, L. A. Rusch, and S. LaRochelle, "Transmission of 50 Gb/s with a Dual Phase-Shift Bragg Grating Silicon Photonic Modulator," in *Optical Fiber Communication Conference*, 2016, p. Th3J.7.
- [23] M. Burla, L. R. Cortés, M. Li, X. Wang, L. Chrostowski, and J. Azaña, "Integrated waveguide Bragg gratings for microwave photonics signal processing," *Opt. Express*, vol. 21, no. 21, p. 25120, Oct. 2013.
- [24] X. Wang, W. Shi, R. Vafaei, N. A. F. Jaeger, and L. Chrostowski, "Silicon-on-insulator Bragg gratings fabricated by deep UV lithography," in *Asia Communications and Photonics Conference and Exhibition*, 2010, pp. 501–502.

- [25] M. Burla, L. R. Cortes, M. Li, X. Wang, L. Chrostowski, and J. Azana, "On-chip ultra-wideband microwave photonic phase shifter and true time delay line based on a single phase-shifted waveguide Bragg grating," in *2013 IEEE International Topical Meeting on Microwave Photonics (MWP)*, 2013, pp. 92–95.
- [26] T. Baba, "Slow light in photonic crystals," *Nat. Photonics*, vol. 2, no. 8, pp. 465–473, 2008.
- [27] K. McGarvey-Lechable, T. Hamidfar, D. Patel, L. Xu, D. V. Plant, and P. Bianucci, "Slow light in mass-produced, dispersion-engineered photonic crystal ring resonators," *Opt. Express*, vol. 25, no. 4, p. 3916, 2017.
- [28] C. Xiang, M. L. Davenport, J. B. Khurgin, P. A. Morton, and J. E. Bowers, "Low-Loss Continuously Tunable Optical True Time Delay Based on Si₃N₄ Ring Resonators," *IEEE J. Sel. Top. Quantum Electron.*, vol. 24, no. 4, pp. 1–9, 2018.
- [29] X. Wang *et al.*, "Continuously tunable ultra-thin silicon waveguide optical delay line," *Optica*, vol. 4, no. 5, p. 507, 2017.
- [30] J.-W. Dong, X.-D. Chen, H. Zhu, Y. Wang, and X. Zhang, "Valley photonic crystals for control of spin and topology," *Nat. Mater.*, vol. 16, no. 3, pp. 298–302, 2017.
- [31] S. Mahmoodian, K. Prindal-Nielsen, I. Söllner, S. Stobbe, and P. Lodahl, "Engineering chiral light-matter interaction in photonic crystal waveguides with slow light," *Opt. Mater. Express*, vol. 7, no. 1, p. 43, 2017.
- [32] L. Jiang and Z. R. Huang, "Integrated Cascaded Bragg Gratings for On-Chip Optical Delay Lines," *IEEE Photonics Technol. Lett.*, vol. 30, no. 5, pp. 499–502, 2018.
- [33] W. Shi, V. Veerasubramanian, D. Patel, and D. V. Plant, "Tunable nanophotonic delay lines using linearly chirped contradirectional couplers with uniform Bragg gratings," *Opt. Lett.*, vol. 39, no. 3, p. 701, 2014.
- [34] Z. Zhang *et al.*, "Electromagnetically induced transparency-like effect in microring-Bragg gratings based coupling resonant system," *Opt. Express*, vol. 24, no. 22, p. 25665, 2016.
- [35] A. Yariv, P. Yeh, and A. Yariv, *Photonics: optical electronics in modern communications*. Oxford University Press, Inc., 2006.
- [36] L. Chrostowski and M. E. Hochberg, *Silicon photonics design*. Cambridge University Press, 2015.
- [37] S. Akiyama *et al.*, "Compact PIN-Diode-Based Silicon Modulator Using Side-Wall-Grating Waveguide," *IEEE J. Sel. Top. Quantum Electron.*, vol. 19, no. 6, pp. 74–84, 2013.
- [38] H. Bahrami, H. Sepehrian, C. S. Park, L. A. Rusch, and W. Shi, "Time-Domain Large-Signal Modeling of Traveling-Wave Modulators on SOI," *J. Light. Technol.*, vol. 34, no. 11, pp. 2812–2823, Jun. 2016.
- [39] X. Wang, "Silicon photonic waveguide Bragg gratings," University of British Columbia, 2013.
- [40] A. D. Simard and S. LaRochelle, "A Dynamic Model of Silicon Bragg Grating Modulators," *IEEE J. Sel. Top. Quantum Electron.*, vol. 22, no. 6, pp. 107–115, 2016.
- [41] J. Lauzon, S. LaRochelle, and F. Ouellette, "Numerical analysis of all-optical switching of a fiber Bragg grating induced by a short-detuned pump pulse," *Opt. Commun.*, vol. 92, no. 4–6, pp. 233–239, 1992.
- [42] E. Kalnay, *Atmospheric modeling, data assimilation, and predictability*. Cambridge University Press, 2003.
- [43] D. Patel, "Design, Analysis, and Performance of a Silicon Photonic Traveling Wave Mach-Zehnder Modulator," McGill University, 2014.
- [44] Y. Hinakura, Y. Terada, H. Arai, and T. Baba, "Electro-Optic Phase Matching in Si Photonic Crystal Slow Light Modulator," in *Advanced Photonics 2018 (BGPP, IPR, NP, NOMA, Sensors, Networks, SPPCom, SOF)*, 2018, p. IW3B.6.
- [45] Y. Hinakura, Y. Terada, H. Arai, and T. Baba, "Electro-optic phase matching in a Si photonic crystal slow light modulator using meander-line electrodes," *Opt. Express*, vol. 26, no. 9, p. 11538, Apr. 2018.
- [46] A. Shakoor, K. Nozaki, E. Kuramochi, K. Nishiguchi, A. Shinya, and M. Notomi, "Compact 1D-silicon photonic crystal electro-optic modulator operating with ultra-low switching voltage and energy," *Opt. Express*, vol. 22, no. 23, p. 28623, Nov. 2014.